Caving 2026 – A van As, D Cumming-Potvin & J Wesseloo (eds)

doi:10.36487/ACG_repo/2645_18

# Simulating cave growth, primary fragmentation and flow using a mesh-free approach

**Vinh Thanh Le [a], Tien Viet Nguyen [a], Murat Karakus [b,*], Giang Dinh Nguyen [c], Chris Chester [d], Matthew Musolino [d], Ha Hong Bui [a]**

[a] *Department of Civil and Environmental Engineering, Monash University, Australia*

[b] *School of Chemical Engineering, Mining Engineering, Adelaide University, Australia*

[c] *School of Civil Engineering and Construction Management, Adelaide University, Australia*

[d] *Carrapateena, BHP, Australia*

## Abstract

*Block-and-panel caving operations rely on the controlled propagation of rock mass failure. However, the mechanisms governing cave advance, fragmentation and stability remain unclear. Observations from physical modelling and field studies indicate that cave growth may occur through either gradual damage accumulation or discrete fracture banding. However, a unified numerical explanation of these behaviours is still limited. This paper applies a mechanical smoothed particle hydrodynamics (SPH) modelling approach with an energy-regularised damage-plasticity constitutive model to simulate the complete rock caving process. The approach enables continuous representation of fracture initiation, progressive fragmentation and gravity-driven material flow, while accounting for stress path–dependent failure under both compressive and tensile loading conditions.*

*Numerical simulations of centrifuge-scale caving experiments successfully reproduce key caving features observed in practice, including stepped cave advance via parallel fracture bands, transient arching, airgap formation and eventual roof collapse. The results demonstrate that fracture banding emerges from the interaction between undercut geometry, loss of confinement and stress path transitions during cave propagation. Parametric analyses indicate that the draw/undercut schedule primarily controls early-stage cave development by controlling the spatial-temporal pattern of support removal and stress redistribution, thereby promoting either a continuous cave back or spatially concentrated cave growth above isolated undercut zones. In parallel, the initial dilation angle, $\psi_0$, provides a strong constitutive control on caveability: lower values favour progressive banded failure, whereas higher values promote stable arching and delayed cave advance. The modelling results provide mechanistic insight into cave propagation and stability and demonstrate the capability of the SPH-damage-plasticity approach to capture fracture development, primary fragmentation/material detachment, and post-failure flow in a single mesh-free simulation.*

**Keywords:** *block caving, fracture banding, cave propagation, smoothed particle hydrodynamics, SPH, damage-plasticity modelling*

## 1 Introduction

Cave mining relies on the controlled propagation of the rock mass above an undercut, progressing from fracture initiation to fragmentation and ultimately gravity-driven flow. However, the mechanisms that govern cave advance and stability remain incompletely understood. Two end-member behaviours are commonly used to interpret cave propagation: continuous damage accumulation that produces a smooth damage profile behind the cave back (the Duplancic conceptual model) (Brown 2002), and discrete fracture banding,

* Corresponding author. Email address: murat.karakus@adelaide.edu.au

in which damage localises into approximately parallel bands and drives stepped cave advance (Cumming-Potvin et al. 2016, 2018a). A central challenge is to identify the mechanisms controlling the transition between these behaviours as confinement is progressively removed and the stress path evolves through mixed tensile shear and compression shear regimes. However, a unified numerical explanation that connects these responses remains limited in the literature.

Our recent smoothed particle hydrodynamics (SPH) simulations, the first continuum-based approach to reproduce these competing caving mechanisms, showed that material dilatancy, represented by the initial dilation angle $\psi_0$, is a decisive control: a high $\psi_0$ promotes stable arching consistent with a continuous damage response, whereas a low $\psi_0$ favours progressive failure through discrete fracture bands (Le et al. 2025a). Yet caveability is not governed by constitutive behaviour alone (Hebert & Sharrock 2018). The draw/undercut schedule governs the sequence of confinement loss and stress redistribution around the undercut and can therefore influence where fracture bands initiate, how fractured and fragmented zones coalesce, and how rapidly the cave back propagates.

Motivated by this interaction, this paper uses our validated SPH modelling approach with an energy-regularised damage-plasticity model to reproduce centrifuge-scale caving and to quantify the combined effects of draw/undercut schedule and $\psi_0$ on fracture band development and cave growth. In this study, the term (primary) fragmentation refers to the detachment and separation of fractured rock zones from the cave back/front during cave propagation, rather than the quantification of fragment-size distribution or secondary fragmentation during draw. We first simulate a benchmark centrifuge test to establish a baseline caving response and demonstrate the model's capability to capture the full process of cave growth, fragmentation and flow. We then conduct a parametric study to isolate and quantify how the draw schedule and $\psi_0$ jointly control fracture band formation and cave propagation. Caveability is evaluated using both the evolution of damage patterns and a quantitative relationship between the critical cave back height $H_c$ and undercut span $B$.

# 2 An energy-regularised damage-plasticity model

This section summarises the energy-regularised damage-plasticity model proposed by Le et al. (2025b), which is implemented in the SPH approach in this study to simulate the full rock caving process (Section 4).

## 2.1 Convention and definition

Einstein summation is used throughout this paper. Tensile stresses are taken as positive and compressive stresses as negative. The first stress invariant is $I_1 = \sigma_{kk}$. The deviatoric stress is $s_{ij} = \sigma_{ij} - \sigma_{kk}\delta_{ij}/3$, and its second invariant is $J_2 = s_{ij}s_{ij}/2$. Hydrostatic pressure and equivalent shear stress are defined as $p = -\sigma_{kk}/3$ and $q = \sqrt{3J_2}$, respectively. Total strain is additively decomposed into elastic and plastic parts: $\varepsilon_{ij} = \varepsilon_{ij}^e + \varepsilon_{ij}^p$. Micro-cracking is represented by a scalar damage variable $D \in [0,1]$, where $D = 0$ denotes intact material and $D = 1$ corresponds to complete damage.

## 2.2 Model formulation

*The generalised constitutive relation between stress and strain is expressed as:*

$$\sigma_{ij} = C_{ijkl}(\varepsilon_{kl} - \varepsilon_{kl}^p) \tag{1}$$

where:

$\varepsilon_{kl}$ = total strain tensors

$\varepsilon_{kl}^p$ = plastic strain tensors

$C_{ijkl}$ = secant elastic stiffness tensor, defined as follows:

$$C_{ijkl} = \{[(1-s) + sH(-\sigma_{kk})]K - 2(1-s)G/3\}\delta_{ij}\delta_{kl} + (1-s)G[\delta_{ik}\delta_{jl} + \delta_{il}\delta_{jk}] \tag{2}$$

where:

| | | |
|---|---|---|
| $K = E/[3(1-2\nu)]$ | = | bulk modulus |
| $G = E/[2(1+\nu)]$ | = | shear modulus |
| $E$ | = | Young's modulus |
| $\nu$ | = | Poisson's ratio |
| $\delta$ | = | Kronecker delta function |
| $H(-\sigma_{kk})$ | = | Heaviside function, accounting for stiffness recovery under compression |
| $s = rD$ | = | $r \in [0,1]$ is the residual stiffness parameter at full damage: $r = 0$ implies no degradation, whereas $r = 1$ gives complete stiffness loss ($G = 0$, and $K = 0$ in tension) when $D = 1$. |

The yield surface is defined in hyperbolic form as:

$$y = -(c + \mu p) + \sqrt{q^2 + (c - \mu p_t)^2} = 0 \tag{3}$$

where:

| | | |
|---|---|---|
| $c$ | = | cohesion, defined as $c(D) = c_0(1-D)$, with $c_0$ the initial cohesion |
| $p_t$ | = | tensile strength under isotropic tension, defined as $p_t(D) = p_{t0}(1-D)$, where $p_{t0}$ is the initial isotropic tensile strength |
| $\mu = tan(\phi)$ | = | friction coefficient, with a damage-dependent friction angle $\phi(D) = \phi_r + (\phi_p - \phi_r)(1-D)$, where $\phi_p$ and $\phi_r$ are the peak and residual friction angles, respectively. |

A non-associated flow rule is adopted:

$$\dot{\varepsilon}_{kl}^{p} = \dot{\lambda}\frac{\partial g_p}{\partial \sigma_{kl}} \tag{4}$$

with plastic potential

$$g_p = -(c + \beta p) + \sqrt{q^2 + (c - \beta p_t)^2} \tag{5}$$

where:

| | | |
|---|---|---|
| $\dot{\lambda}$ | = | damage-plastic multiplier rate |
| $\beta$ | = | $tan(\psi)$, with $\psi$ the dilation angle evolving as $\psi(D) = \psi_0(1-D)$, where $\psi_0$is the initial value. |

Model closure is achieved by specifying the rate of the isotropic scalar damage variable $\dot{D}$ as follows:

$$\dot{D} = \sum(\dot{D}_t + \dot{D}_c) \tag{6}$$

where:

| | | |
|---|---|---|
| $\dot{D}_t = \eta_{D_t}(1-D)\sqrt{2\dot{\varepsilon}_{kl}^{p}\dot{\varepsilon}_{kl}^{p}/3}$ | = | incremental damage in tension |
| $\dot{D}_c = \eta_{D_c}(1-D)\sqrt{2\dot{\varepsilon}_{kl}^{p}\dot{\varepsilon}_{kl}^{p}/3}$ | = | incremental damage in compression |
| $\eta_{D_t}$ and $\eta_{D_c}$ | = | constant model parameters that govern energy dissipation and corresponding damage growth in tension and compression, respectively; their calibration procedure is described in Le et al. (2025b). |

In the numerical implementation, the constitutive model is integrated using a semi-implicit stress return algorithm with sub-stepping to improve stability and accuracy, particularly in the high-damage regimes encountered during rock caving simulations. Full implementation details are provided in Le et al. (2025b).

# 3 Numerical modelling inputs

This section presents the centrifuge experiments of Cumming-Potvin (2018) and the corresponding SPH model set-up and identified constitutive inputs. In the centrifuge tests, a weakly cemented concrete block was accelerated to 80 g to reproduce gravity-driven caving. Undercutting and progressive loss of confinement were simulated by supporting the specimen base with 5 hydraulic pistons that were sequentially retracted to mimic material extraction. A schematic of the test configuration and the associated stress distribution is shown in Figures 1a and 1b.

To mimic these conditions, the SPH simulations use a 2D plane strain assumption. The Cartesian origin $O$ is located at the bottom-left corner of the specimen, as shown in Figures 1a and 1b. The initial particle spacing is $dx = 0.003$ m, leading to 25,368 material particles and 1,007 boundary particles. A Wendland Quintic C4 kernel is adopted, with smoothing length $h = 1.3dx$ and kernel support radius $2h = 0.0078$ m (Le et al. 2025a). Depth-dependent external pressures ($\sigma_v$ and $\sigma_h$) are applied to the outermost material particle layer on the top, left and right boundaries, consistent with the experiment. Boundary conditions are imposed using 3 layers beneath the specimen (B–$BC_1$) and an additional 3-layer boundary (B–$BC_2$, 500 mm long) located 150 mm away to prevent particles from leaving the computational domain during the stage due to stress material flow stage. All boundary particles remain fixed with no-slip conditions, except the pistons, which move vertically downward to reproduce extraction. The piston motion follows the sequence $P1 \rightarrow P2 \rightarrow P3 \rightarrow P4 \rightarrow P5$ with a vertical speed of 0.05 m/s, zero horizontal velocity and a 5 mm lead distance between successive pistons. The piston displacement histories over the simulation time are shown in Figure 1c. The simulation timestep is $dt = 7.8 \times 10^{-7}$ s.

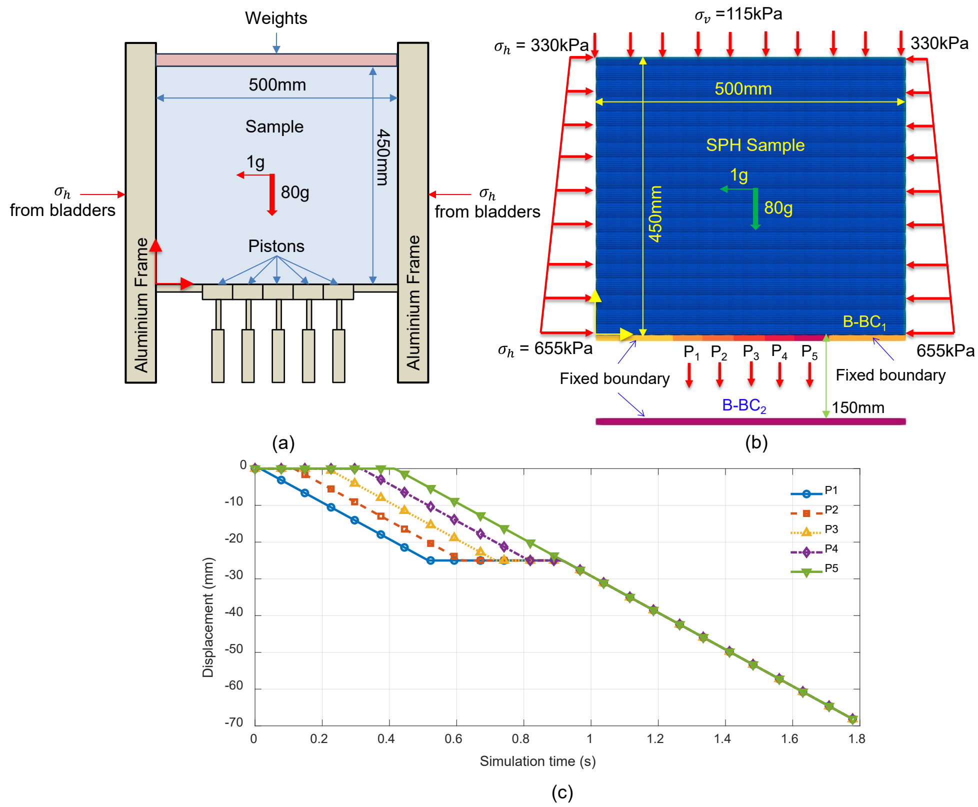


**Figure 1 (a) Schematic of centrifuge test design (reproduced from Cumming-Potvin 2018); (b) Loading and boundary conditions used in SPH simulation set-up; (c) Undercut procedure (piston displacement histories) adopted in the simulation**

The constitutive parameters of the energy-regularised damage-plasticity model (Section 2) are summarised in Table 1. Details of the calibration procedure are provided in Le et al. (2025b). In addition, material heterogeneity is incorporated using a Weibull distribution, following Le et al. (2025a).

**Table 1 Model parameters used for the damage-plasticity model**

| Constitutive model parameter | Value |
|---|---|
| Young's modulus, $E$ | 350 MPa |
| Poisson's ratio, $\nu$ | 0.1 |
| Initial cohesion, $c_0$ | 120 kPa |
| Initial isotropic tensile strength, $p_{t0}$ | 20 kPa |
| Peak friction angle, $\phi_p$ | 50° |
| Residual friction angle, $\phi_r$ | 60° |
| Initial dilation angle, $\psi_0$ | 35° |
| Tensile fracture energy, $G_{Ft}$ | 10 Pa.m |
| Tensile damage parameter, $\eta_{Dt}$ | 28.93 |
| Compressive damage parameter, $\eta_{Dc}$ | 20 |
| Residual stiffness parameter, $r$ | 0.75 |

# 4 Numerical results and discussions

## 4.1 Full caving evolution and governing failure mechanisms

This section demonstrates the capability of the SPH numerical approach combined with an energy-regularised damage-plasticity constitutive model to reproduce the full caving evolution observed in centrifuge tests (Cumming-Potvin 2018), from fracture initiation and progressive fragmentation to post-failure material flow. Figure 2 compares the SPH predictions with the centrifuge observations and shows that the simulations capture the key stages of cave development. At the onset of undercutting, the cave expands laterally and vertically, forming a rounded cave profile accompanied by distinct airgap formation, consistent with the experimental observation (Figure 2a). As undercutting proceeds, the model reproduces progressive fracture and fragmentation through the emergence of approximately parallel fracture bands ahead of the cave front, leading to stepped cave advance as successive bands form. These bands typically initiate near piston corners, propagate upward while remaining largely parallel, and drive progressive enlargement of the cave and associated formation of new and closure of existing voids, in close qualitative agreement with the experiments (Figures 2b–d).

In this simulation, SPH offers a practical advantage over conventional mesh-based continuum approaches (Cumming-Potvin et al. 2018b) because it can naturally accommodate very large deformation, progressive fragmentation and post-failure material flow, as illustrated in Figures 2e and 2f. Once the material has lost most of its cohesion and tensile resistance ($D \approx 1$) and piston extraction becomes sufficiently large, the fragmented material is discharged from the specimen and accumulates against the B–$C_2$ boundary. Overall, Figure 2 confirms that combining the energy-regularised damage-plasticity model with SPH enables qualitative reproduction of the full caving sequence, from fracture and fragmentation to gravity-driven flow. It is noted that the time $t$ reported in the simulation figures represents the numerical progression of the staged undercutting process rather than a direct one-to-one correspondence with the experimental time. Since the adopted constitutive model is rate independent, the piston velocity was selected to reproduce the sequence of support removal while keeping inertial effects limited. Therefore, the comparison with the centrifuge observations focuses on the evolution of cave geometry, fracture band development, airgap formation and material flow, rather than the exact timing of events observed in the experiments.

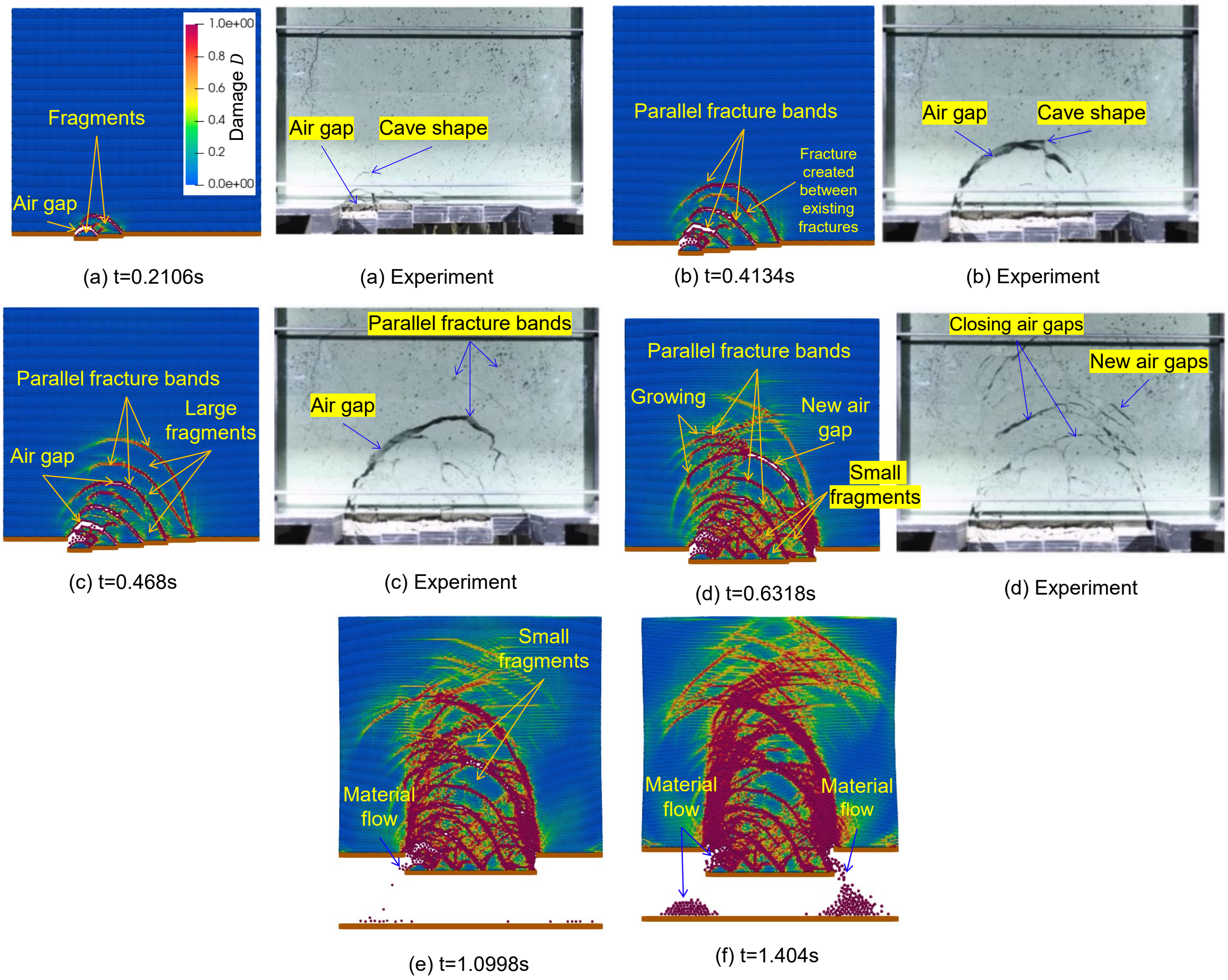


**Figure 2 SPH simulation snapshots of the full caving evolution – fracture initiation, progressive fragmentation and gravity-driven material flow – at selected times, compared with the centrifuge observations from Test 4 reported by Cumming-Potvin (2018) after Le et al. (2025a)**

Figure 3 elucidates the governing failure mechanisms by tracking the accumulated tensile and compressive damage variables, $D_t$ and $D_c$, during staged undercutting. In the early stage, when the first 2 pistons are withdrawn (Figure 3$a_1$ and $b_1$), $D_t$ is markedly larger than $D_c$, indicating that tensile shear processes dominate. This aligns with the limited fragmentation observed at this time: damage remains confined to small zones above P1 and P2, while the rock mass above the cave back stays largely intact and continues to sustain the high confinement imposed by the 80 g field, the vertical surcharge and the lateral stresses. Under these conditions, stress relaxation around the undercut promotes the initiation and upward propagation of fracture bands primarily through tensile shear mechanisms.

At the subsequent stage (Figures 3$a_2$ and 3$b_2$), $D_t$ remains dominant overall, except for a localised region above piston P4 where $D_c$ becomes comparatively larger. As undercutting advances and additional pistons are retracted, the unsupported span increases and larger fragments form, bound by parallel fracture bands that extend into the middle and upper parts of the specimen (Figures 3$a_3$–$a_4$ and Figures 3$b_3$–$b_4$). The resulting reduction in load-bearing capacity above the cave back triggers airgap closure (Figure 3$b_3$), which limits confinement relief within the fracture bands and drives a transition toward compression-dominated damage. Accordingly, $D_c$ becomes prevalent at later times, particularly in the middle and upper parts of the specimen (Figures 3b$_3$–b$_4$). Overall, these results confirm that cave growth in the centrifuge test in this study is inherently mixed mode, involving a tensile shear–controlled banding stage due to stress relaxation, followed by a compression shear–dominated response as confinement remains high, underscoring the need for an advanced constitutive model capable of capturing both regimes. In this regard, our energy-regularised damage-plasticity model combined with SPH approach provides a robust option for simulating the whole caving process.

(a) Accumulated tensile damage $D_t$

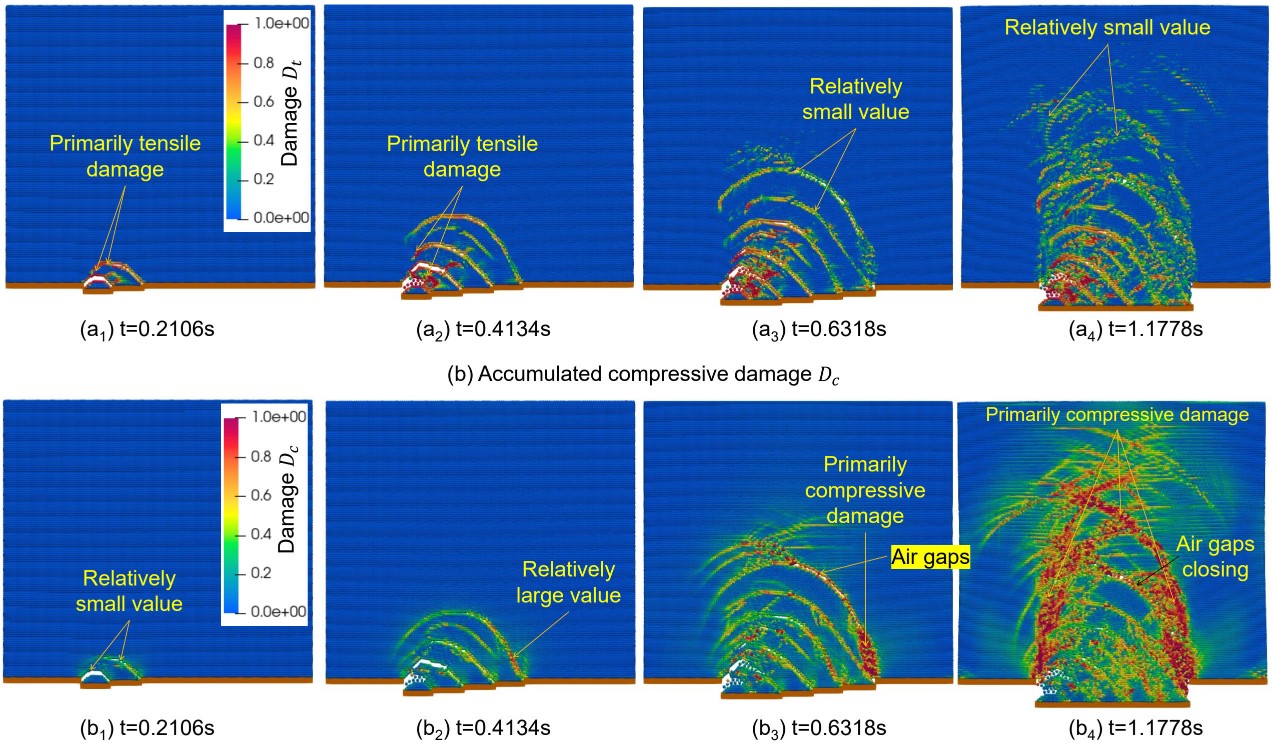


**Figure 3 Evolution of damage during staged undercutting. (a) Accumulated tensile damage, $D_t$; (b) Accumulated compressive damage, $D_c$, at selected times (after Le et al. 2025a)**

## 4.2 Undercut sequence effects on fracture band development and cave growth

In the baseline simulation (Figures 2 and 3), undercutting is generated by sequentially retracting 5 pistons (see Figure 1c), which progressively removes the basal support and drives stress redistribution in the sample. Since this redistribution controls where fractures initiate and how the cave front advances, the piston withdrawal order can influence the timing and spatial pattern of parallel fracture band formation and, consequently, the evolving cave geometry. This section, therefore, examines how alternative undercut (piston) sequences affect fracture band development and cave growth, and compares the resulting caving responses. To quantify this sensitivity, we perform 2 additional simulations with different withdrawal sequences. Figure 4 defines these draw schedules through the piston displacement histories. The original schedule retracts pistons in the order P1 → P2 → P3 → P4 → P5, whereas Sequence II follows P1 → P3 → P5 → P2 → P4 and Sequence III follows P2 → P4 → P1 → P3 → P5. Although these schedules impose different timing and spatial patterns of support removal across the base, they are designed to achieve a comparable final undercut extent (Figure 4). The corresponding caving responses are then compared with the baseline case in Figure 5.

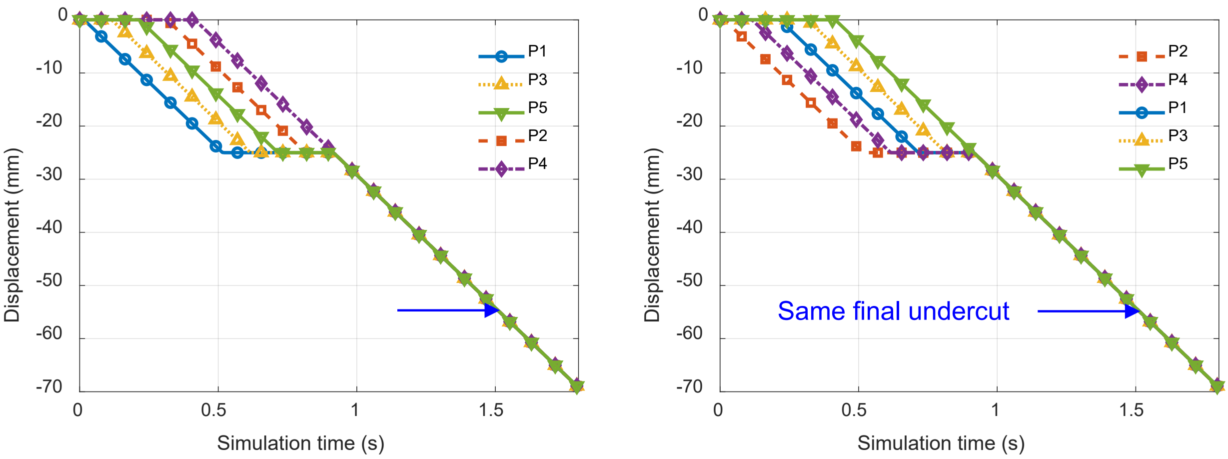


(b)

**Figure 4 Piston displacement histories defining the alternative undercut sequences. (a) Sequence II, $P1 \rightarrow P3 \rightarrow P5 \rightarrow P2 \rightarrow P4$; (b) Sequence III, $P2 \rightarrow P4 \rightarrow P1 \rightarrow P3 \rightarrow P5$; all sequences are designed to reach a comparable final undercut extent**

Figure 5 shows that the undercut sequence primarily affects the early-stage cave back evolution, while the late-stage cave geometry becomes similar once the full undercut is established. For Sequence I (original undercut procedure), the cave back grows relatively continuously as the undercut width increases in a spatially progressive manner. Fracture bands form near the active piston corners and propagate upward in an approximately parallel pattern, producing a steady, stepwise advance of the cave front (Figure 5$a_1$–$a_4$). In contrast, sequences II and III produce pronounced local cave growth at early times (Figure 5$b_1$–$b_2$ and Figure 5$c_1$ –$c_2$). This behaviour occurs because the initial piston withdrawals are spatially non-adjacent, creating small, disconnected undercut zones. Consequently, damage and banding remain limited to isolated zones above the active pistons rather than forming a continuous cave back across the entire undercut width. As additional pistons are withdrawn, these isolated damaged regions interact and merge, leading to a more continuous cave back and the emergence of fracture band patterns similar to those in Sequence I (Figures 5$b_3$–$b_4$ and Figures 5$c_3$–$c_4$). By $t = 1.482$ s, cave growth and damage patterns are comparable across all 3 sequences (Figures 5$a_5$, $b_5$, $c_5$), indicating that the late-stage response is governed mainly by the final undercut geometry. Overall, the results show that the mechanical SPH simulation reproduces the expected influence of undercut sequence on cave development. Different sequences mainly affect the early-stage response, particularly the onset, spatial distribution and coalescence of fracture bands, whereas the late-stage cave geometry is largely governed by the extent of the final undercut. Since the influence of draw/undercut sequence on cave propagation is already well established, this section is interpreted as a verification and sensitivity study. It also provides the necessary background for Section 4.3, where the combined effects of initial dilation angle and undercut sequence are investigated.

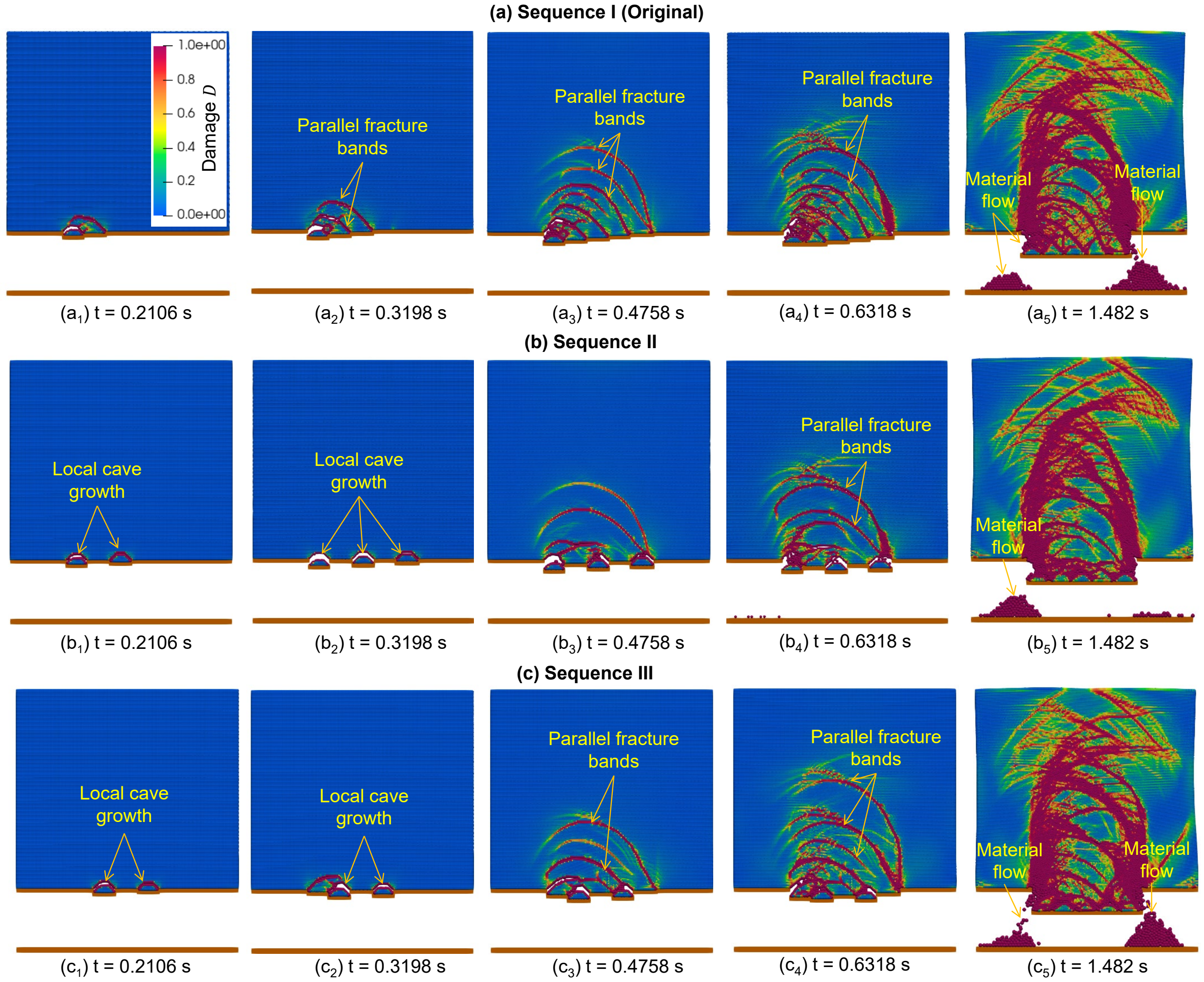


**Figure 5 Caving response under different piston retraction sequences. Damage field snapshots at representative times for (a) Sequence I (baseline); (b) Sequence II; (c) Sequence III**

## 4.3 Combined effects of initial dilation angle and draw/undercut schedule on caveability

In our previous study (Le et al. 2025a), we demonstrated that the initial dilation angle $\psi_0$ strongly influences caveability by controlling whether the cave propagates progressively or stabilises through arching. Here, we extend that analysis by examining how $\psi_0$ interacts with the draw/undercut schedule, because the withdrawal sequence governs both the spatial-temporal pattern of basal support removal and the resulting stress redistribution around the undercut. As shown in Section 4.2, different sequences can produce either a more continuous cave back or early-stage cave growth confined to isolated zones above non-adjacent pistons. This analysis is not intended to re-establish the general importance of draw/undercut scheduling alone, which is already well recognised. Instead, it examines how the initial dilation angle interacts with different undercut sequences to influence fracture band development, cave back propagation and arch stability. This combined effect is investigated using a mechanical SPH approach capable of capturing fracture development, primary fragmentation/material detachment and post-failure flow within a single simulation.

To isolate the role of $\psi_0$, Figure 6 compares cave evolution under the same drawing schedule (Sequence II) for $\psi_0 = 25°$, $45°$ and $55°$. For the lower-dilatancy case ($\psi_0 = 25°$), the cave advances readily through progressive banded failure and fragmentation: after initial damage near the undercut (Figure 6a$_1$), multiple fracture bands develop and extend upward (Figure 6a$_2$), leading to substantial cave back growth and extensive fragmentation and material flow by $t = 1.1778$ s (Figure 6a$_3$). When $\psi_0$ increases to $45°$, cave propagation becomes noticeably more stable. The early-stage response remains limited to the vicinity of the undercut (Figure 6b$_1$), and by $t = 0.6318$ s, an arch-like zone becomes evident (Figure 6b$_2$), which restricts upward damage propagation and promotes the development of a large airgap at later times (Figure 6b$_3$). For the highest dilatancy ($\psi_0 = 55°$), this stabilising trend is further amplified: a pronounced stable arch forms by $t = 0.6318$s (Figure 6c$_2$) and persists at $t = 1.1778$s (Figure 6c$_3$), accompanied by a very large airgap and strongly delayed cave back advance. Mechanistically, increasing $\psi_0$ enhances dilatant shear resistance, promotes arching and shifts the response away from progressive fracture band–driven advance towards a more stable arch. In this sense, high $\psi_0$ favours a cave back behaviour closer to a Duplancic-type continuous damage accumulation ahead of the cave back, whereas low $\psi_0$ promotes stepped propagation governed by discrete fracture bands (Le et al. 2025 a). It should be noted that the selected initial dilation angles are relatively high compared with conventional estimates. However, high mobilised dilation angles have been reported for weak/soft rocks under low confinement. For example, Zhao & Cai (2010) showed that Moura coal can exhibit dilation angles of approximately $40° - 50°$, while weak, medium-grained sandstone can reach about $55°$. Alejano & Alonso (2005) also emphasised that dilation depends on confinement and accumulated plastic deformation, rather than being a constant material parameter. In this study, the specimen is a weak concrete/cemented material subjected to relatively low confinement; therefore, relatively high initial dilation angles can be reasonably assumed as effective parameters for the present sensitivity analysis. Nevertheless, these values are treated as effective initial dilation parameters for sensitivity analysis, not general design values. The simplified evolution rule $\psi = \psi_0(1 - D)$ in this study does not fully capture stress- and path-dependent dilation; therefore, further experimental calibration is required for practical applications.

Figure 7 examines the influence of the draw/undercut schedule at a fixed dilation angle ($\psi_0 = 45°$) by comparing the evolution of the damage field across the 3 withdrawal sequences. For Sequence I (baseline), the cave back develops relatively continuously as the undercut widens progressively; fracture bands initiate and coalesce to form a coherent, advancing cave front (Figures 7a$_1$–a$_3$). In contrast, Sequences II and III exhibit early-stage cave growth that remains spatially concentrated above the initially activated pistons (Figures 7b$_1$ and c$_1$). This occurs because the first 2 piston withdrawals are spatially non-adjacent, so the undercut initially comprises small, disconnected zones. Consequently, damage and banding develop above these isolated extraction zones rather than forming a continuous cave back across the entire width of the undercut (Figures 7b$_2$ and c$_2$). As additional pistons are withdrawn, the damaged regions begin to interact and merge, and the resulting fracture band patterns become more comparable across the sequences (Figures 7b$_3$ and c$_3$). Notably, even at the same moderate $\psi_0$, the late-time responses still differ: Sequence I evolves toward more extensive banded failure (higher caveability; Figure 7a$_3$), whereas Sequence II tends toward stabilised arching with reduced upward propagation (lower caveability; Figure 7b$_3$). Overall, these results indicate that the draw/undercut schedule primarily governs the progression and timing of cave development, while its interaction with dilatancy determines whether the cave advances through progressive fracture bands or stabilises through arching.

Finally, Figure 8 provides a quantitative measure of caveability by relating the critical cave back height $H_c$ to the undercut span/width $B$ (Figure 8a). To ensure a fair comparison of cave back geometry across cases, $H_c$ is extracted at the same set of simulation times, t = 0.117, 0.2184, 0.312, 0.4134 and 0.936 s, which correspond to $B$ = 50, 100, 150, 200 and 250 mm, respectively. Across all sequences, $H_c$ increases with $B$, but the growth rate depends strongly on $\psi_0$, demonstrating a clear constitutive control on cave propagation (Figures 8b–d). Lower dilation angles ($\psi_0 = 25°$ to $35°$) consistently produce larger $H_c$ at a given undercut span, indicating easier upward cave propagation through fracture band development and fragmentation. In contrast, higher dilation ($\psi_0 = 55°$) yields markedly smaller $H_c$ and delayed growth even at large $B$, consistent with stable arching and reduced caveability observed in Figures 6b and 6c. The drawing schedule modifies these trends by controlling how effectively the undercut is mobilised: Sequence I typically shows a smoother increase of $H_c$ with $B$ (Figure 8b), whereas sequences II and III tend to suppress cave back growth at smaller spans due to spatially confined early undercutting, followed by a sharper increase once damaged regions merge and a coherent cave front develops (Figures 8c–d). Overall, Figure 8 confirms that caveability is governed by the combined effects of dilatancy (promoting either progressive fracture band stepping or stable arching) and drawing schedule (controlling the spatial development and coalescence of cave growth).

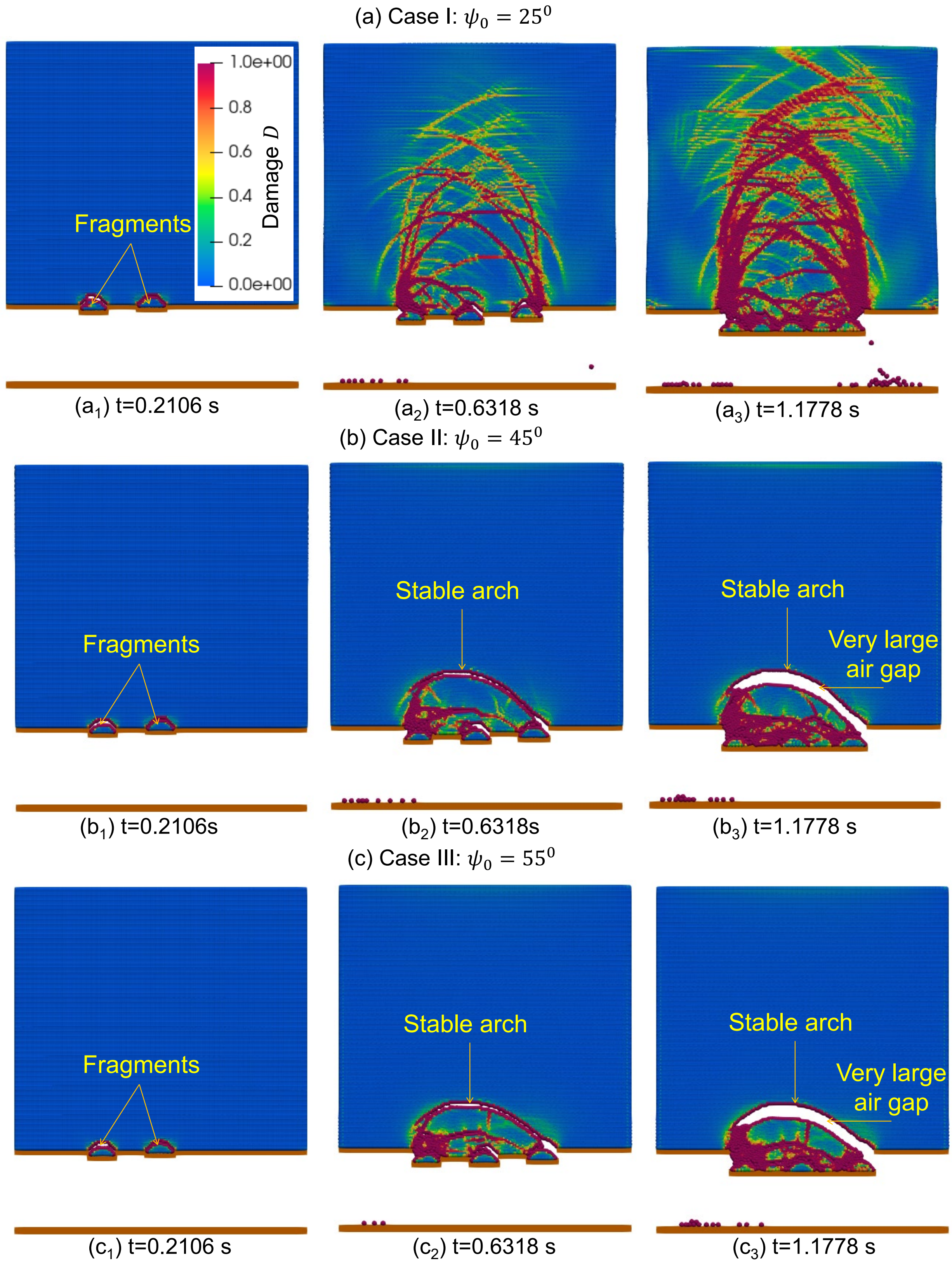


**Figure 6 Caving response under different initial dilation angle for Sequence II: damage field snapshots at representative times for (a) $\psi_0 = 25^0$; (b) $\psi_0 = 45^0$; (c) $\psi_0 = 55^0$**

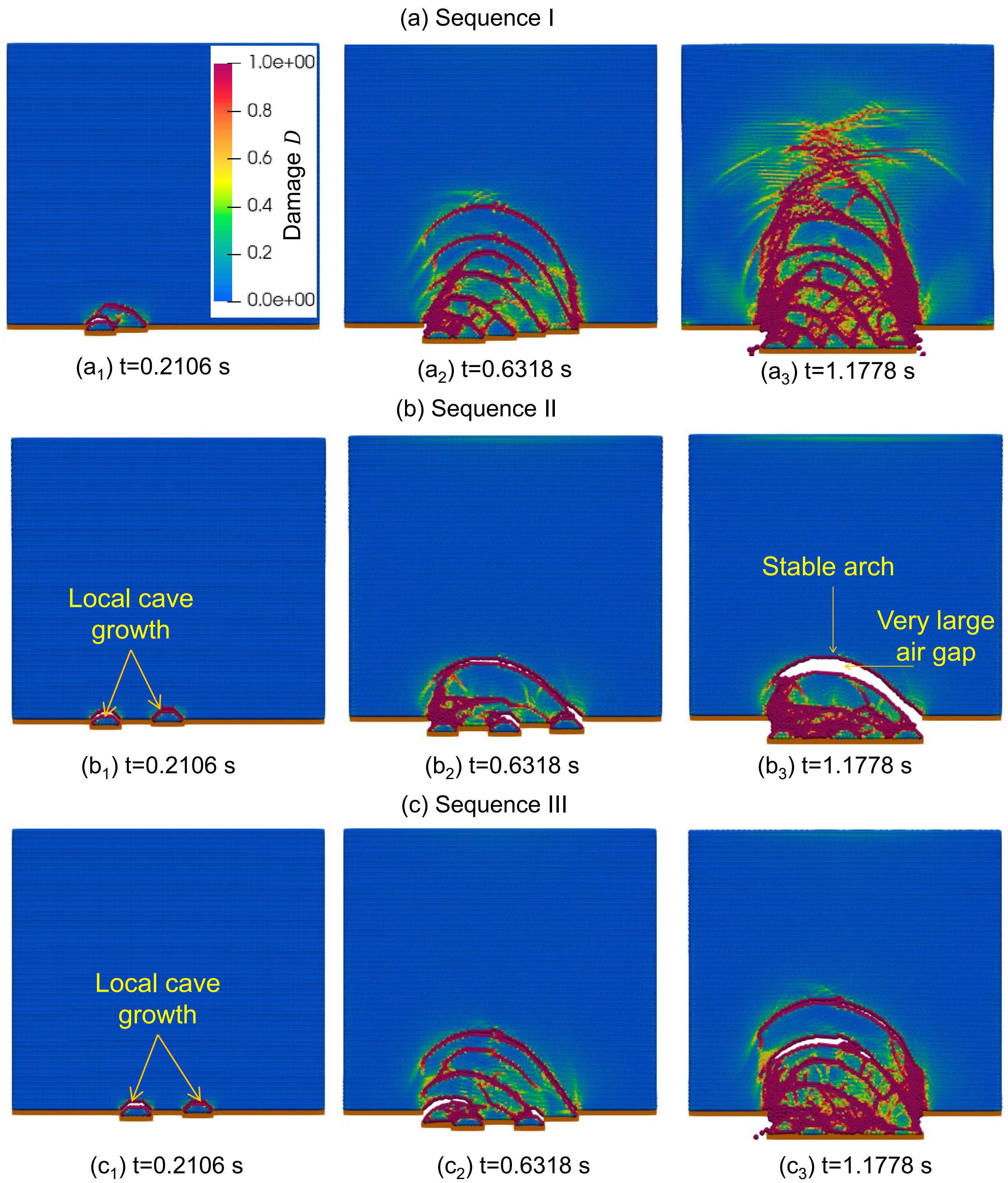


**Figure 7 Caving response under different piston retraction sequences using the same initial dilation angle $\psi_0 = 45^0$. Damage field snapshots at representative times for (a) Sequence I (baseline); (b) Sequence II; (c) Sequence III**

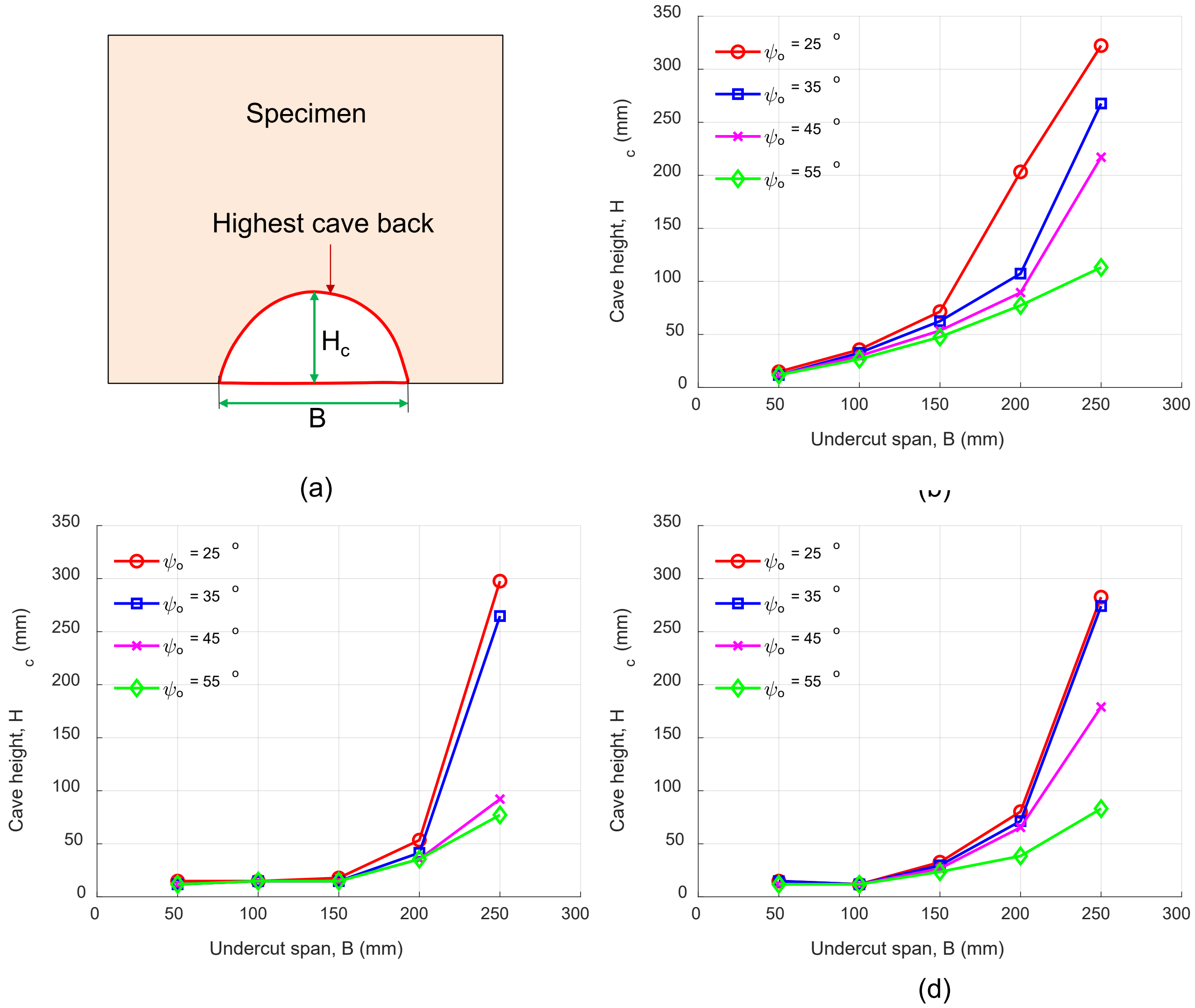


**Figure 8** **(a) Definition of critical height ($H_c$) of the cave back and undercut span/width ($B$); (b to d) Relationships $H_c - B$ under different initial dilation angles for sequences I, II and III, respectively**

# 5 Conclusion

This study uses the SPH approach combined with an energy-regularised damage-plasticity model to examine the combined effects of draw/undercut schedule (piston withdrawal sequence) and initial dilation angle $\psi_0$ on caveability. The baseline simulations reproduced key centrifuge test features, including parallel fracture bands, stepped cave advance, airgap formation, fragmentation and gravity-driven flow, demonstrating that the approach can capture the full caving process under mixed tensile shear and compression shear stress paths. The draw schedule primarily controls the early-stage progression of cave development: spatially progressive undercutting promotes more continuous cave back growth, whereas non-adjacent initial withdrawals generate spatially concentrated cave growth above isolated undercut zones and delay the formation of a coherent cave front. The initial dilation angle $\psi_0$ provides a strong constitutive control on caveability, with lower $\psi_0$ promoting progressive fracture band propagation and larger critical cave back heights, while higher $\psi_0$ encourages stable arching, larger airgaps, and reduced upward cave propagation. The $H_c$-$B$ relationships confirm that caveability is governed by the combined action of dilatancy and draw/undercut schedule: sequencing controls the spatial development and coalescence of damaged regions, while $\psi_0$ determines whether the system favours fracture band stepping or arch stabilisation. The selected $\psi_0$ values should be interpreted as effective initial dilation parameters for the weak cemented material and low-confinement centrifuge conditions considered in this study, rather than general design values for field-scale rock masses. The simplified evolution rule $\psi = \psi_0(1 - D)$ does not fully capture the stress-dependent and path-dependent dilation behaviour of intact rocks and rock masses; therefore, further experimental calibration is required for practical applications.

## Acknowledgement

Support from the Australian Research Council through projects LP200100038 (Karakus, Nguyen, Bui), LP220200792 (Karakus, Nguyen, Bui) and FT200100884 (Bui) is gratefully acknowledged. Part of this research was conducted with the assistance of resources and services from the Monash Advanced Research Computing Hybrid (MonARCH) and the National Computational Infrastructure (NCMAS-2025-66, NCMAS-2026-70).

## References

Alejano, LR & Alonso, E 2005, ‘Considerations of the dilatancy angle in rocks and rock masses’, *International Journal of Rock Mechanics and Mining Sciences*, vol. 42, no. 4, pp. 481–507, https://doi.org/10.1016/j.ijrmms.2005.01.003

Brown, ET 2002, *Block Caving Geomechanics*, Julius Kruttschnitt Mineral Research Centre, The University of Queensland, Indooroopilly, Queensland.

Cumming-Potvin, D 2018, *An Extended Conceptual Model of Caving Mechanics*, PhD thesis, The University of Western Australia, Perth.

Cumming-Potvin, D, Wesseloo, J, Jacobsz, SW & Kearsley, E 2016, ‘Fracture banding in caving mines’, *Journal of the Southern African Institute of Mining and Metallurgy*, vol. 116, no. 8, pp. 753–761, https://doi.org/10.17159/2411-9717/2016/v116n8a7

Cumming-Potvin, D, Wesseloo, J, Jacobsz, SW & Kearsley, E 2018a, ‘A re-evaluation of the conceptual model of caving mechanics’, in Y Potvin & J Jakubec (eds), *Caving 2018: Proceedings of the Fourth International Symposium on Block and Sublevel Caving*, Australian Centre for Geomechanics, Perth, pp. 179–190, https://doi.org/10.36487/ACG_rep/1815_11_Cumming-Potvin

Cumming-Potvin, D, Wesseloo, J, Pierce, ME, Garza-Cruz, T, Bouzeran, L, Jacobsz, SW & Kearsley, E 2018b, ‘Numerical simulations of a centrifuge model of caving’, in Y Potvin & J Jakubec (eds), *Caving 2018: Proceedings of the Fourth International Symposium on Block and Sublevel Caving*, Australian Centre for Geomechanics, Perth, pp. 191–206, https://doi.org/10.36487/ACG_rep/1815_12_Cumming-Potvin

Hebert, Y & Sharrock, G 2018, ‘Three-dimensional simulation of cave initiation, propagation and surface subsidence using a coupled finite difference-cellular automata solution’, in Y Potvin & J Jakubec (eds), *Caving 2018: Proceedings of the Fourth International Symposium on Block and Sublevel Caving*, Australian Centre for Geomechanics, Perth, pp. 151–166, https://doi.org/10.36487/ACG_rep/1815_09_Hebert

Le, VT, Nguyen, TV, Karakus, M, Nguyen, GD & Bui, HH 2025a, ‘SPH-based modelling of the entire rock caving process: insights into failure mechanisms’, *International Journal of Rock Mechanics and Mining Sciences*, vol. 194, 106228, https://doi.org/10.1016/j.ijrmms.2025.106228

Le, VT, Nguyen, TV, Nguyen, NT, Nguyen, GD, Karakus, M & Bui, HH 2025b, ‘A simple 3D damage-plasticity model with energy-based regularisation in SPH for modelling fractured quasi-brittle rocks’, *Rock Mechanics and Rock Engineering*, vol. 58, pp. 9937–9964, https://doi.org/10.1007/s00603-025-04638-x

Zhao, XG & Cai, M 2010, ‘A mobilized dilation angle model for rocks’, *International Journal of Rock Mechanics and Mining Sciences*, vol. 47, no. 3, pp. 368–384, https://doi.org/10.1016/j.ijrmms.2009.12.007